Phonon-induced localization of excitons in molecular crystals from first principles

Antonios M. Alvertis,[1,2,*] Jonah B. Haber,[2] Edgar A. Engel,[3] Sahar Sharifzadeh,[4,5] and Jeffrey B. Neaton[1,2,6,†]

[1] *Materials Sciences Division, Lawrence Berkeley National Laboratory, Berkeley, California 94720, USA*
[2] *Department of Physics, University of California Berkeley, Berkeley, United States*
[3] *Cavendish Laboratory, University of Cambridge, J. J. Thomson Avenue, Cambridge CB3 0HE, United Kingdom*
[4] *Division of Materials Science and Engineering, Boston University, United States*
[5] *Department of Electrical and Computer Engineering, Boston University, United States*
[6] *Kavli Energy NanoScience Institute at Berkeley, Berkeley, United States*

(Dated: August 5, 2023)

The spatial extent of excitons in molecular systems underpins their photophysics and utility for optoelectronic applications. Phonons are reported to lead to both exciton localization and delocalization. However, a microscopic understanding of phonon-induced (de)localization is lacking, in particular how localized states form, the role of specific vibrations, and the relative importance of quantum and thermal nuclear fluctuations. Here we present a first-principles study of these phenomena in solid pentacene, a prototypical molecular crystal, capturing the formation of bound excitons, exciton-phonon coupling to all orders, and phonon anharmonicity, using density functional theory, the *ab initio GW*-Bethe-Salpeter equation approach, finite difference, and path integral techniques. We find that for pentacene zero-point nuclear motion causes uniformly strong localization, with thermal motion providing additional localization only for Wannier-Mott-like excitons. Anharmonic effects drive temperature-dependent localization, and while such effects prevent the emergence of highly delocalized excitons, we explore the conditions under which these might be realized.

Introduction.– Photoexcitation of organic molecular crystals leads to strongly bound electron-hole pairs, or excitons, due to the weak screening of the Coulomb interaction in these systems. Depending on factors such as the size of the molecular building blocks and the spin of the electron-hole pair, exciton radii can vary from those of localized Frenkel excitons [1, 2] to spatially extended excitons that approach the Wannier-Mott limit [3–7]. The spatial extent of these excited states is important to applications of organic semiconductors such as photovoltaics [8] and LEDs [9], since it affects properties including the nature of their interaction with phonons [10], their transport [11] and non-radiative recombination [12].

Critical to affecting the spatial extent of excited states are lattice vibrations, which are generally thought to result in wavefunction localization [13]. Phonons can strongly renormalize one- and two-particle excitation energies of organic systems, influencing the optical gap and the charge carrier mobility [10, 14, 15]. Phonons in these systems have generally been thought to lead to localized excitons that diffuse via, *e.g.*, a Förster or Dexter mechanism [16, 17]. However, it has recently been proposed that in certain well-ordered organic crystals atomic motion can give rise to configurations that favor strong transient exciton delocalization, having a beneficial effect to transport [18–20]. This transient exciton delocalization is similar to transient *charge* delocalization [21–23], wherein phonons lead to configurations with large overlaps between neighboring molecular orbitals [24] and hence highly delocalized states [25].

Despite these insights, a rigorous microscopic understanding of phonon-induced modulations to exciton radii, one that accounts for electron-hole interactions, strong exciton-phonon coupling at finite temperatures [10, 26], and the anharmonicity of low-frequency motions in molecular crystals [27–30], is still lacking. Here we elucidate the microscopic mechanism of exciton localization in extended molecular solids. We employ a first-principles computational framework which captures all aforementioned effects, combining density functional theory (DFT), the Green's function-based *ab initio GW*-Bethe Salpeter equation (BSE) approach for accurately describing exciton effects [31], finite-difference methods for strong exciton-phonon interactions [10, 32], and path integral techniques for describing phonon anharmonicity [33, 34]. We apply this framework to the prototypical molecular crystal pentacene and show that zero-point nuclear motion leads to strong localization of singlet and triplet excitons, reducing their average electron-hole separation by more than a factor of two. Temperature increases further reduce the size of delocalized Wannier-Mott-like excitons, an effect driven by anharmonic phonons. The trends in exciton radii are reflected in the dispersion of their energies in reciprocal space. While highly delocalized excitons do appear at large phonon displacements, anharmonicity reduces the amplitude associated with these motions, suppressing transient delocalization for exciton transport.

System and methods.– We focus on the widely studied molecular crystal pentacene [35], which hosts a delocalized Wannier-Mott-like singlet exciton (Fig. 1a) and a more localized Frenkel-like triplet exciton (Fig. 1b) [7,

* amalvertis@lbl.gov
† jbneaton@lbl.gov

10, 36], for which the effect of phonons is expected to be different. We compute excitons with principal quantum number S and center-of-mass momentum $\boldsymbol{Q}$ using *ab initio* DFT and *GW*-BSE calculations with the Quantum Espresso [37] and BerkeleyGW [38] codes. This involves constructing the electron-hole kernel K^{e-h} and solving the BSE [31, 39] in reciprocal space in the electron-hole basis, namely

$$\begin{aligned}(E_{c\boldsymbol{k}+\boldsymbol{Q}} - E_{v\boldsymbol{k}})A^S_{cv\boldsymbol{k}\boldsymbol{Q}} \\ + \sum_{c'v'\boldsymbol{k}'} \langle c\boldsymbol{k}+\boldsymbol{Q}, v\boldsymbol{k}| K^{e-h} |c'\boldsymbol{k}'+\boldsymbol{Q}, v'\boldsymbol{k}'\rangle A^S_{c'v'\boldsymbol{k}'\boldsymbol{Q}} \\ = \Omega^S_{\boldsymbol{Q}} A^S_{cv\boldsymbol{k}\boldsymbol{Q}},\end{aligned} \tag{1}$$

with input from prior DFT and *GW* calculations. In Eq. 1 the indices c, v define conduction and valence states respectively, $\boldsymbol{k}$ is the crystal momentum, and $A^S_{cv\boldsymbol{k}\boldsymbol{Q}}$ is the amplitude contributed by states c, v with momentum $\boldsymbol{k}$ to the exciton with momentum $\boldsymbol{Q}$. The exciton wavefunction can be written as

$$\Psi^{\boldsymbol{Q}}_S(\boldsymbol{r}_e, \boldsymbol{r}_h) = \sum_{cv\boldsymbol{k}} A^S_{cv\boldsymbol{k}\boldsymbol{Q}} \psi_{c\boldsymbol{k}+\boldsymbol{Q}}(\boldsymbol{r}_e)\psi^*_{v\boldsymbol{k}}(\boldsymbol{r}_h), \tag{2}$$

where $\psi_{n\boldsymbol{k}}$ are the Kohn-Sham wavefunctions. The kernel K^{e-h} consists only of an attractive 'direct' term between electrons and holes for triplets, while for singlets it also includes a repulsive 'exchange' term, giving singlets their greater spatial extent [7, 31]. The energies of the conduction and valence bands in Eq. 1 are obtained within the so-called *GW* approximation [40] from self-energy corrections to DFT Kohn-Sham eigenvalues. This approach has been shown to give highly accurate descriptions of excitons in molecular crystals [7, 10, 36, 41, 42]. The computational details for our DFT and *GW*-BSE calculations are given in Supplemental Material [43] Section S1.

We treat the effect of phonons following Monserrat [32, 44, 45], and in a manner similar in spirit to Zacharias and Giustino [46, 47]. For an observable $\mathcal{O}$ at a temperature T, we compute the ensemble-average in the adiabatic approximation as

$$\langle \mathcal{O}(T) \rangle_{\mathcal{H}} = \frac{1}{Z} \int dX \mathcal{O}(X) e^{-\beta \mathcal{H}}, \tag{3}$$

where the canonical partition function $Z = \int dX e^{-\beta\mathcal{H}}$ involves the configuration space integral $\int dX$ [48]. Non-adiabatic effects to the electron-phonon interactions of organic systems such as pentacene are negligible [49].

The Hamiltonian $\mathcal{H}$ of the system includes electronic and nuclear degrees of freedom in general, and may be approximated at different levels. One approach is to assume nuclear motion to be harmonic, reducing the phonon contribution to the Hamiltonian to the following form,

$$\mathcal{H}^{\text{har}} \equiv \frac{1}{2} \sum_{n,\mathbf{q}} (\nabla^2_{u_{n,\mathbf{q}}} + \omega^2_{n,\mathbf{q}} u^2_{n,\mathbf{q}}), \tag{4}$$

in atomic units. Here, phonons of frequencies ω are labeled by their branch index n and wavevector $\mathbf{q}$. We compute the ensemble-average $\langle \mathcal{O}^{\text{har}} \rangle$ in the Born-Oppenheimer approximation, tracing out all electronic degrees of freedom, using a finite-displacements approach [50, 51] to calculate phonon frequencies $\{\omega_{n,\mathbf{q}}\}$ and eigendisplacements $\{u_{n,\mathbf{q}}\}$, and then drawing N random samples $\{X^{\text{har}}_i\}$ from the multivariate Gaussian phonon distribution and calculating the observables of interest $\{\mathcal{O}(X^{\text{har}}_i)\}$. $\langle \mathcal{O}^{\text{har}} \rangle$ is then simply computed as the average of its value at the samples

$$\langle \mathcal{O}^{\text{har}} \rangle = \lim_{N\to\infty} \frac{1}{N} \sum_{i=1}^{N} \mathcal{O}(X^{\text{har}}_i). \tag{5}$$

Eqs. 4 and 5 are exact apart from the adiabatic and harmonic approximations, and the description of phonon effects on any observable $\mathcal{O}$ in Eq. 5 is non-perturbative [26].

The use of the harmonic approximation in molecular crystals can lead to unphysical results, due to highly anharmonic behavior of low-frequency phonons [27, 29]. In this work, we account for this anharmonicity by employing path-integral molecular dynamics (PIMD) which are rendered computationally tractable using the surrogate machine-learning (ML) potential V^{ML} from Refs. [27, 52], constructed to reproduce the potential energy surface (PES) from first-principles density functional theory (DFT) calculations. The modified phonon Hamiltonian

$$\mathcal{H}^{\text{anhar}} \equiv \sum_{i=1}^{N_a} \frac{\hat{\mathbf{p}}^2_i}{2m_i} + V^{\text{ML}}(\hat{\mathbf{r}}_1, \ldots, \hat{\mathbf{r}}_{N_a}) \tag{6}$$

is used to run PIMD simulations at reduced computational cost, for a cell of N_a atoms, with nucleus i having a mass m_i, and $\hat{\mathbf{p}}_i$, $\hat{\mathbf{r}}_i$ its momentum and position operators respectively. We then draw random samples from the PIMD trajectories, and use these to compute vibrational averages of observables, analogously to Eq. 5, namely

$$\langle \mathcal{O}^{\text{anhar}} \rangle = \lim_{N\to\infty} \frac{1}{N} \sum_{i=1}^{N} \mathcal{O}(X^{\text{anhar}}_i). \tag{7}$$

Our simulations use a $2 \times 1 \times 1$ supercell of pentacene ($N_a = 144$ atoms), capturing the effect of phonons at Γ and at the band-edge X on observables. Phonons beyond Γ and X have a minor effect on pentacene optical properties as discussed in Supplemental Material [43] Section S1.C.

To quantify exciton localization, we study two observ-

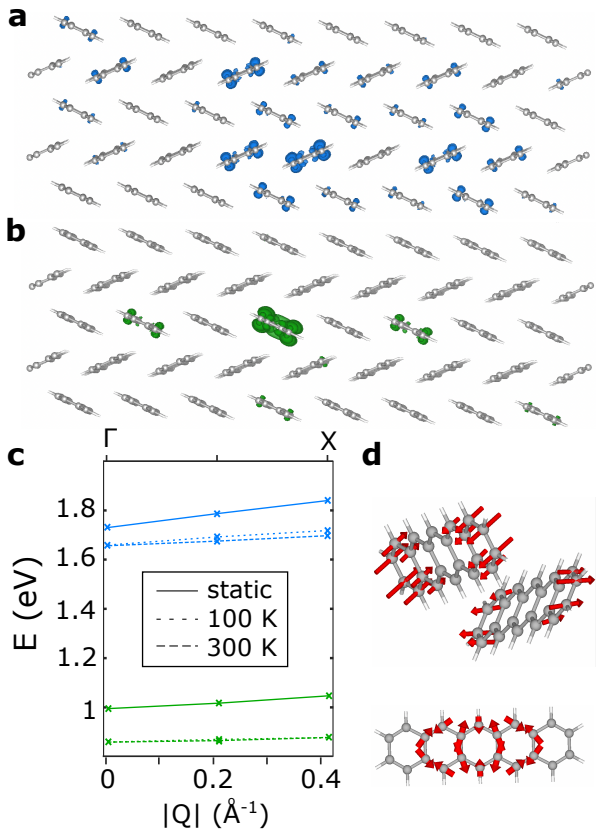

FIG. 1. Isosurfaces of electron distributions of singlet (blue, panel **a**) and triplet (green, panel **b**) excitons for a hole fixed at the center of the plotted area, and corresponding dispersions (panel **c**, same color scheme) in molecular crystals. A typical low-frequency (top) and high-frequency (bottom) phonon of pentacene is shown in panel **d**.

ables $\mathcal{O}$. The first are the exciton energies at finite center-of-mass momentum, $\Omega^S_{\boldsymbol{Q}}$, obtained through solving the BSE (Eq. 1). The second is the average electron-hole separation for each excitation S, which we refer to as the exciton radius $r_{\rm exc}$. This is obtained by post-processing the BSE solution Ψ_S, as discussed elsewhere [53] and in Supplemental Material [43] Section S1. To determine the exciton radius, we compute the electron-hole correlation function as defined in Ref. [53], namely

$$F_S(\boldsymbol{r}) = \int_V d\boldsymbol{r}_h |\Psi_S^{\boldsymbol{Q}=0}(\boldsymbol{r}_e = \boldsymbol{r}_h + \boldsymbol{r}, \boldsymbol{r}_h)|^2, \qquad (8)$$

where V the volume of the primitive cell. $F_S(\boldsymbol{r})$ describes the probability of finding the electron-hole pair at a distance of $\boldsymbol{r} = \boldsymbol{r}_e - \boldsymbol{r}_h$, and is computed as a discrete sum over hole positions. The average exciton radius for a given atomic configuration is then

$$r_{\rm exc} = \int d|\boldsymbol{r}| F_S(|\boldsymbol{r}|)|\boldsymbol{r}|. \qquad (9)$$

Having described the main quantities in our computational framework, we may summarize it as follows. We generate displaced configurations $X_i^{\rm har}$ within the harmonic approximation using a finite differences approach, and $X_i^{\rm anhar}$ within the anharmonic distribution through PIMD employing a previously-developed ML potential. The *ab initio* BSE, Eq. 1, is solved at these configurations, followed by a calculation of the exciton radius via Eq. 9. We then compute the vibrational averages using Eqs. 5 and 7. Details of the convergence of the vibrational averages, the ML potential, and PIMD simulations, are given in Supplemental Material [43] Section S1.

Results.– We first discuss exciton properties obtained from solving the BSE without consideration of phonons. We refer to these clamped-ion solutions as the 'static' case. Fig. 1 shows an isosurface of the electron density for the first singlet (S_1, blue, panel **a**) and triplet (T_1, green, panel **b**) exciton, for a hole fixed at the center of the visualized region. As shown previously [7, 10, 36], the singlet is significantly more delocalized than the triplet, which results in bands that are more dispersive in reciprocal space [7, 42], as shown in Fig. 1c. We plot the exciton energies along the path $\Gamma \to X$ in the Brillouin zone, corresponding to the dominant packing direction of the pentacene crystal. Table I summarizes the bandwidth $W = \Omega(X) - \Omega(\Gamma)$ of the two excitons, as well as the width $\Delta = \Omega(\mathbf{Q} = 0.4\ \text{Å}^{-1}) - \Omega(\mathbf{Q} = 0.1\ \text{Å}^{-1})$, the values of the exciton momentum chosen to accommodate comparison to recent experiments [54]. We see from our static calculations that the singlet bandwidth is more than twice that of the triplet.

We now include the effect of phonons on the exciton band structures along $\Gamma \to X$ at 100 K and 300 K, within the harmonic and anharmonic distributions, and visualize the results in Fig. 1c when including anharmonic effects. There are two broad categories of phonons in molecular crystals, corresponding to low-frequency intermolecular and high-frequency intramolecular motions, visualized in Fig. 1d. While the former are predominantly activated when going from 100 K to 300 K, the latter have significant zero-point energies $\hbar\omega/2$. Including 100 K phonon effects red-shifts both singlet and triplet exciton energies and flattens their dispersions, as shown in Fig. 1c and Table I. This effect is larger for the triplet, which is more localized and therefore more impacted by high-frequency intra-molecular modes. However, increasing the temperature to 300 K has no effect on the triplet, since there are negligible additional contributions from intramolecular modes at these temperatures and the modulations of intermolecular distances by lower-frequency phonons hardly affect this localized state. In contrast, the delocalized singlet red-shifts further, and its dispersion flattens by an additional 18 meV. Our results for the singlet width Δ at 100 K are in excellent agreement with recent experiments [54], as summarized in Table I. Our predicted decrease of the singlet width Δ by 13 meV when increasing the temperature from 100 K to 300 K underestimates the experimental decrease of

	$W^{\mathrm{anhar}}(\mathrm{S}_1)$ (meV)	$W^{\mathrm{har}}(\mathrm{S}_1)$ (meV)	$W^{\mathrm{anhar}}(\mathrm{T}_1)$ (meV)	$\Delta^{\mathrm{anhar}}(\mathrm{S}_1)$ (meV)	$\Delta^{\mathrm{exp}}(\mathrm{S}_1)$ (meV) [54]
static	110	110	52	80	– – –
100 K	59	67	18	43	44
300 K	41	76	19	30	23

TABLE I. The effect of phonons on the dispersion width $W = \Omega(X) - \Omega(\Gamma)$ for the first singlet Ω_S and triplet Ω_T excitons of pentacene, and on the width $\Delta = \Omega(\mathbf{Q} = 0.4\ \text{Å}^{-1}) - \Omega(\mathbf{Q} = 0.1\ \text{Å}^{-1})$ for the singlet.

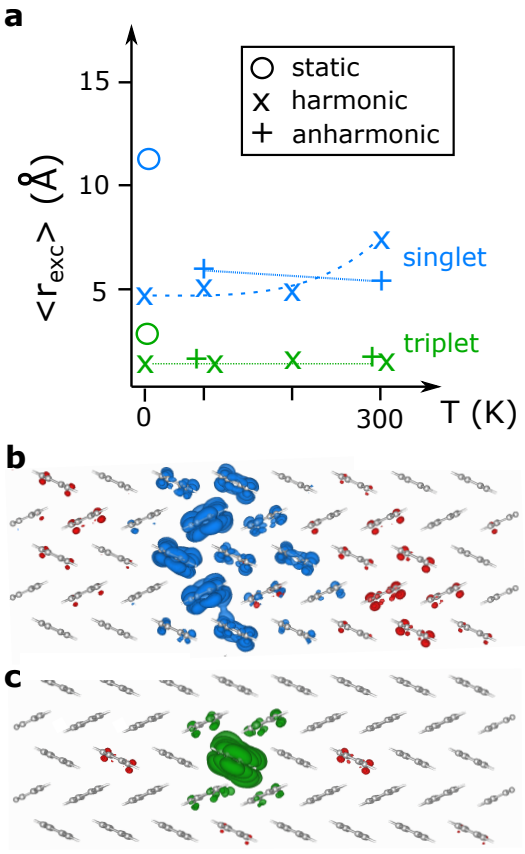

FIG. 2. Singlet (blue) and triplet (green) exciton radii within the different cases and temperatures (panel **a**). Representative configuration showing electronic isosurfaces for fixed hole positions, indicating localization of the singlet (triplet) at 0 K towards the region in blue (green), shown in panel **b** (panel **c**). Red represents electronic wavefunction amplitude that disappears in the presence of phonons.

21 meV, largely due to ignoring thermal expansion in our calculation, which reduces Δ by a further 6 meV within this temperature range, see Supplemental Material [43] Section S2. Interestingly, we see in Table I that the harmonic approximation predicts an *increase* of the singlet bandwidth with increasing temperature, contrary to our calculations including anharmonic effects using PIMD and to experiment, a point that we return to below.

The changes in the width of the exciton dispersions suggest phonon-induced modulations of real-space exciton properties, which are zero-point dominated for the triplet, and which have significant temperature dependence for the singlet. We highlight the connection between the dispersion modulations and real-space exciton properties by computing vibrational averages of the exciton radii at a range of temperatures. The results are presented in Fig. 2 for the singlet (blue) and triplet (green) within the harmonic approximation and including anharmonic effects. Let us first comment on the harmonic case. Compared to the static limit (circles), the radii in the presence of phonons at 0 K are renormalized by more than a factor of two. For the singlet, the static value of 11.2 Å for its radius reduces to 4.9 Å, while the static triplet radius of 2.7 Å reduces to 1.2 Å. To visualize this we present in Fig. 2b and Fig. 2c differential plots for isosurfaces of the electron density once a hole is placed at a high-probability position in the unit cell. Specifically, we plot the difference between the electronic density of the case without phonons and that of a typical atomic configuration at 0 K. Red indicates amplitude vanishing due to phonons, while blue and green indicate areas where the singlet and triplet wavefunction respectively gain amplitude, demonstrating their tendency to localize.

When increasing the temperature to 300 K within the harmonic approximation there is no change to the triplet exciton radius, in agreement with our expectation of the effect of phonons on the triplet exciton dispersion. The singlet however exhibits delocalization, with its radius increasing substantially to the average value of 6.96 Å, consistent with the increase of the singlet bandwidth with temperature in the harmonic case. Upon including anharmonic effects, triplet radii agree with the harmonic case; however, for the singlet the results are qualitatively different, and we recover the expected behavior of decreasing singlet radius with increasing temperature. All vibrational averages and errors for the exciton radii are given in Section S7 of the Supplemental Material [43].

The discrepancy between the harmonic and anharmonic cases is due to configurations with highly delocalized excitons within the harmonic approximation, with radii as large as 31 Å at 300 K. Such configurations are shown in Supplementary Material [43] Section S5, and their inclusion in the thermal averages of Eq. 5 for the radii leads to the observed temperature-induced increase of $\langle r_{\mathrm{exc}} \rangle$ in Fig. 2a. To understand why such configurations are not present within the anharmonic case, we plot in Fig. 3a the difference between the phonon root mean squared displacement $\sqrt{\langle u^2 \rangle}$ of the two distributions at 300 K. We find that a low-frequency acoustic mode, corresponding to a sliding along the z-axis of adjacent pentacene molecules, is significantly over-displaced

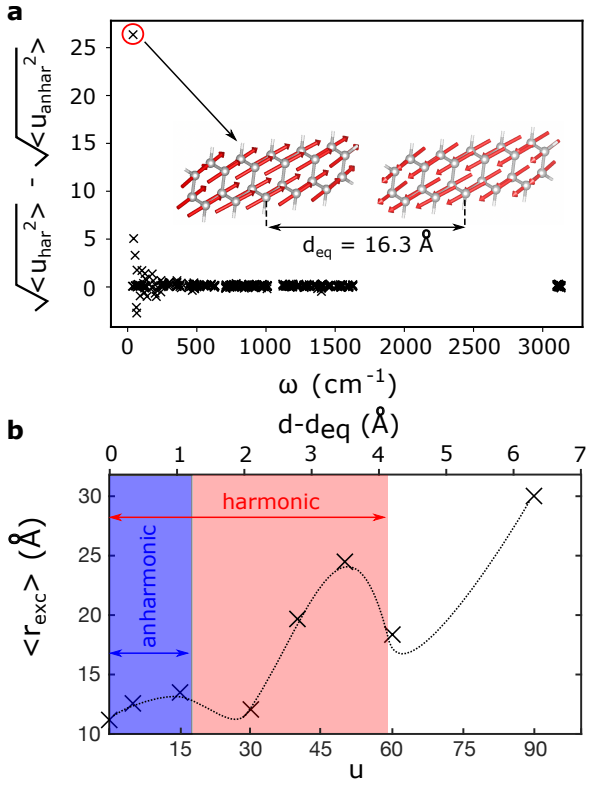

FIG. 3. The difference between the RMS displacement of phonons in the harmonic and anharmonic distributions of pentacene (panel **a**). Singlet exciton radii (panel **b**) along the highly anharmonic phonon shown in panel **a**. Phonon displacements u are given in units of their zero-point width $1/\sqrt{2\omega_{q\nu}}$ [32]. The dotted line in **b** is a guide to the eye.

in the harmonic case at $\boldsymbol{q} = X$. Anharmonic terms alter the PES associated with this phonon, limiting its average amplitude at room temperature, as shown in Supplementary Material [43] Fig. S3, in agreement with known cases where the harmonic approximation breaks down in molecular crystals [27, 29, 30]. We confirm that the overdisplacement of this phonon within the harmonic approximation leads to the temperature-induced singlet delocalization observed in Fig. 2a, by computing the singlet radius as a function of amplitude of this mode, as visualized in Fig. 3b. The blue and red regions indicate the maximum range of displacements which are accessible within the anharmonic and harmonic distributions respectively, due to thermal excitation of phonons at 300 K. The harmonic approximation leads to configurations with highly delocalized excitons of radii as large as 25 Å. The dependence of the exciton radius on the phonon displacement is non-monotonic due to the oscillating π orbital overlap between neighboring pentacene molecules [55].

While highly delocalized excitons may appear at certain nuclear configurations, anharmonicity prevents accessing these, as seen in Fig. 3b. However, such configurations could appear out of equilibrium, *e.g.* due to photoexcitation, upon relaxation to the excited state PES minimum. For pentacene, the minimum of the singlet exciton PES along the anharmonic acoustic mode lies far from the 'delocalized' region of Fig. 3b (see Supplemental Material [43] Section S6), it is thus unlikely that for this and similar systems transiently delocalized excitons may be accessed, even outside equilibrium.

Conclusions.– We have presented a first-principles study of the effect of phonons on the dispersion and radii of excitons in the prototypical molecular crystal pentacene. Zero-point nuclear motion uniformly causes substantial localization of excitons, manifesting as a flattening of the exciton dispersion in reciprocal space. Wannier-Mott-like singlet excitons also exhibit additional temperature-activated localization due to their stronger coupling to low-frequency phonons, with anharmonic effects being critical in capturing this effect and preventing transient exciton delocalization. Anharmonic low-frequency phonons are common in molecular materials [27] and can couple to singlets when these approach the Wannier-Mott limit, in a manner which is in turn determined by the size [10] and packing [56] of the molecular building blocks. Our work lays foundations for a deep understanding and controlled enhancement of exciton transport in molecular crystals, for example by suppressing anharmonicity through chemical modifications [57].

We thank Sivan Refaely-Abramson for useful discussions. This work was primarily supported by the Theory FWP, which provided *GW* and *GW*-BSE calculations and analysis of phonon effects, and the Center for Computational Study of Excited-State Phenomena in Energy Materials (C2SEPEM), which provided advanced codes, at the Lawrence Berkeley National Laboratory, funded by the U.S. Department of Energy, Office of Science, Basic Energy Sciences, Materials Sciences and Engineering Division, under Contract No. DE-AC02-05CH11231. SS acknowledges funding from the U.S. National Science Foundation (NSF) under grant number DMR-1847774. Computational resources were provided by the National Energy Research Scientific Computing Center (NERSC).

[1] J. Frenkel, On the transformation of light into heat in solids. i, Phys. Rev. **37**, 17 (1931).
[2] J. Frenkel, On the transformation of light into heat in solids. ii, Phys. Rev. **37**, 1276 (1931).
[3] G. H. Wannier, The structure of electronic excitation levels in insulating crystals, Phys. Rev. **52**, 191 (1937).
[4] N. F. Mott, Conduction in polar crystals. II. The conduction band and ultra-violet absorption of alkali-halide crystals, Trans. Faraday Soc. **34**, 500 (1938).
[5] P. Cudazzo, M. Gatti, and A. Rubio, Excitons in molecular crystals from first-principles many-body perturbation theory: Picene versus pentacene, Phys. Rev. B **86**,

1 (2012).
[6] P. Cudazzo, M. Gatti, A. Rubio, and F. Sottile, Frenkel versus charge-transfer exciton dispersion in molecular crystals, Phys. Rev. B **88**, 1 (2013).
[7] P. Cudazzo, F. Sottile, A. Rubio, and M. Gatti, Exciton dispersion in molecular solids, Journal of Physics Condensed Matter **27**, 10.1088/0953-8984/27/11/113204 (2015).
[8] A. Distler, C. J. Brabec, and H. J. Egelhaaf, Organic photovoltaic modules with new world record efficiencies, Progress in Photovoltaics: Research and Applications **29**, 24 (2021).
[9] S. Reineke, F. Lindner, G. Schwartz, N. Seidler, K. Walzer, B. Lüssem, and K. Leo, White organic light-emitting diodes with fluorescent tube efficiency., Nature **459**, 234 (2009).
[10] A. M. Alvertis, R. Pandya, L. A. Muscarella, N. Sawhney, M. Nguyen, B. Ehrler, A. Rao, R. H. Friend, A. W. Chin, and B. Monserrat, Impact of exciton delocalization on exciton-vibration interactions in organic semiconductors, Phys. Rev. B **102**, 081122 (2020).
[11] J. Aragó and A. Troisi, Dynamics of the excitonic coupling in organic crystals, Physical Review Letters **114**, 1 (2015).
[12] G. Kupgan, X. K. Chen, and J. L. Brédas, Molecular Packing in the Active Layers of Organic Solar Cells Based on Non-Fullerene Acceptors: Impact of Isomerization on Charge Transport, Exciton Dissociation, and Nonradiative Recombination, ACS Applied Energy Materials **4**, 4002 (2021).
[13] P. W. Anderson, Absence of diffusion in certain random lattices, Phys. Rev. **109**, 1492 (1958).
[14] F. Brown-Altvater, G. Antonius, T. Rangel, M. Giantomassi, C. Draxl, X. Gonze, S. G. Louie, and J. B. Neaton, Band gap renormalization, carrier mobilities, and the electron-phonon self-energy in crystalline naphthalene, Phys. Rev. B **101**, 1 (2020).
[15] G. Schweicher, G. D'Avino, M. T. Ruggiero, D. J. Harkin, K. Broch, D. Venkateshvaran, G. Liu, A. Richard, C. Ruzié, J. Armstrong, A. R. Kennedy, K. Shankland, K. Takimiya, Y. H. Geerts, J. A. Zeitler, S. Fratini, and H. Sirringhaus, Chasing the "Killer" Phonon Mode for the Rational Design of Low-Disorder, High-Mobility Molecular Semiconductors, Advanced Materials **31**, 10.1002/adma.201902407 (2019).
[16] S. Athanasopoulos, E. V. Emelianova, A. B. Walker, and D. Beljonne, Exciton diffusion in energetically disordered organic materials, Phys. Rev. B **80**, 1 (2009).
[17] L. Sudha Devi, M. K. Al-Suti, C. Dosche, M. S. Khan, R. H. Friend, and A. Köhler, Triplet energy transfer in conjugated polymers. I. Experimental investigation of a weakly disordered compound, Phys. Rev. B **78**, 1 (2008).
[18] A. J. Sneyd, T. Fukui, D. Paleček, S. Prodhan, I. Wagner, Y. Zhang, J. Sung, S. M. Collins, T. J. Slater, Z. Andaji-Garmaroudi, L. R. MacFarlane, J. D. Garcia-Hernandez, L. Wang, G. R. Whittell, J. M. Hodgkiss, K. Chen, D. Beljonne, I. Manners, R. H. Friend, and A. Rao, Efficient energy transport in an organic semiconductor mediated by transient exciton delocalization, Science Advances **7**, 10.1126/sciadv.abh4232 (2021).
[19] S. Giannini, W.-T. Peng, L. Cupellini, D. Padula, A. Carof, and J. Blumberger, Exciton transport in molecular organic semiconductors boosted by transient quantum delocalization, Nature Communications **13**, 1 (2022).
[20] A. J. Sneyd, D. Beljonne, and A. Rao, A New Frontier in Exciton Transport : Transient Delocalization, Journal of Physical Chemistry Letters **13**, 6820 (2022).
[21] S. Fratini, D. Mayou, and S. Ciuchi, The transient localization scenario for charge transport in crystalline organic materials, Advanced Functional Materials **26**, 2292 (2016), 1505.02686.
[22] Y. Zhang, C. Liu, A. Balaeff, S. S. Skourtis, and D. N. Beratan, Biological charge transfer via flickering resonance, Proceedings of the National Academy of Sciences of the United States of America **111**, 10049 (2014).
[23] D. N. Beratan, Why Are DNA and Protein Electron Transfer So Different?, Annual Review of Physical Chemistry **70**, 71 (2019).
[24] A. Troisi, G. Orlandi, and J. E. Anthony, Electronic interactions and thermal disorder in molecular crystals containing cofacial pentacene units, Chemistry of Materials **17**, 5024 (2005).
[25] S. Giannini, A. Carof, M. Ellis, H. Yang, O. G. Ziogos, S. Ghosh, and J. Blumberger, Quantum localization and delocalization of charge carriers in organic semiconducting crystals, Nature Communications **10**, 1 (2019).
[26] B. Monserrat, E. A. Engel, and R. J. Needs, Giant electron-phonon interactions in molecular crystals and the importance of nonquadratic coupling, Phys. Rev. B **92**, 1 (2015).
[27] A. M. Alvertis and E. A. Engel, Importance of vibrational anharmonicity for electron-phonon coupling in molecular crystals, Phys. Rev. B **105**, 1 (2022).
[28] H. Seiler, M. Krynski, D. Zahn, S. Hammer, Y. W. Windsor, T. Vasileiadis, J. Pflaum, R. Ernstorfer, M. Rossi, and H. Schwoerer, Nuclear dynamics of singlet exciton fission: a direct observation in pentacene single crystals, Science Advances **7**, eabg0869 (2021).
[29] J. H. Fetherolf, P. Shih, and T. C. Berkelbach, Conductivity of an electron coupled to anharmonic phonons, arXiv (2022).
[30] M. Rossi, P. Gasparotto, and M. Ceriotti, Anharmonic and Quantum Fluctuations in Molecular Crystals: A First-Principles Study of the Stability of Paracetamol, Phys. Rev. Lett. **117**, 115702 (2016).
[31] M. Rohlfing and S. G. Louie, Electron-hole excitations and optical spectra from first principles, Phys. Rev. B **62**, 4927 (2000), 0406203v3 [arXiv:cond-mat].
[32] B. Monserrat, Electron – phonon coupling from finite differences, Journal of Physics Condensed Matter **30** (2018).
[33] V. Kapil, J. Behler, and M. Ceriotti, High order path integrals made easy, The Journal of Chemical Physics **145**, 234103 (2016).
[34] M. Ceriotti, M. Parrinello, T. E. Markland, and D. E. Manolopoulos, Efficient stochastic thermostatting of path integral molecular dynamics, J. Chem. Phys. **133**, 124104 (2010).
[35] S. Haas, B. Batlogg, C. Besnard, M. Schiltz, C. Kloc, and T. Siegrist, Large uniaxial negative thermal expansion in pentacene due to steric hindrance, Phys. Rev. B **76**, 1 (2007).
[36] S. Refaely-Abramson, F. H. Da Jornada, S. G. Louie, and J. B. Neaton, Origins of Singlet Fission in Solid Pentacene from an ab initio Green's Function Approach, Physical Review Letters **119**, 1 (2017), 1706.01564.
[37] P. Giannozzi, S. Baroni, N. Bonini, M. Calandra, R. Car, C. Cavazzoni, D. Ceresoli, G. L. Chiarotti, M. Cococ-

cioni, I. Dabo, A. Dal Corso, S. Fabris, G. Fratesi, S. de Gironcoli, R. Gebauer, U. Gerstmann, C. Gougoussis, A. Kokalj, M. Lazzeri, L. Martin-Samos, N. Marzari, F. Mauri, R. Mazzarello, S. Paolini, A. Pasquarello, L. Paulatto, C. Sbraccia, S. Scandolo, G. Sclauzero, A. P. Seitsonen, A. Smogunov, P. Umari, and R. M. Wentzcovitch, QUANTUM ESPRESSO: a modular and open-source software project for quantum simulations of materials, Journal of Physics: Condensed Matter **21**, 395502 (2009).

[38] J. Deslippe, G. Samsonidze, D. A. Strubbe, M. Jain, M. L. Cohen, and S. G. Louie, BerkeleyGW: A massively parallel computer package for the calculation of the quasiparticle and optical properties of materials and nanostructures, Computer Physics Communications **183**, 1269 (2012), 1111.4429.

[39] D. Y. Qiu, G. Cohen, D. Novichkova, and S. Refaely-Abramson, Signatures of Dimensionality and Symmetry in Exciton Band Structure: Consequences for Exciton Dynamics and Transport, Nano Letters **21**, 7644 (2021).

[40] M. S. Hybertsen and S. G. Louie, Electron correlation in semiconductors and insulators: Band gaps and quasiparticle energies, Phys. Rev. B **34**, 5390 (1986).

[41] T. Rangel, K. Berland, S. Sharifzadeh, F. Brown-Altvater, K. Lee, P. Hyldgaard, L. Kronik, and J. B. Neaton, Structural and excited-state properties of oligoacene crystals from first principles, Phys. Rev. B **93**, 1 (2016).

[42] T. Lettmann and M. Rohlfing, Finite-momentum excitons in rubrene single crystals, Phys. Rev. B **104**, 1 (2021).

[43] See supplemental material at [url will be inserted by the production group] which includes references [10, 27, 34, 36–38, 41, 44, 52, 53, 58–68] for computational details.

[44] B. Monserrat, Vibrational averages along thermal lines, Phys. Rev. B **93**, 1 (2016), 1512.06377.

[45] B. Monserrat, Correlation effects on electron-phonon coupling in semiconductors: Many-body theory along thermal lines, Phys. Rev. B **93**, 10.1103/PhysRevB.93.100301 (2016), 0703642 [astro-ph].

[46] M. Zacharias and F. Giustino, One-shot calculation of temperature-dependent optical spectra and phonon-induced band-gap renormalization, Phys. Rev. B **94**, 10.1103/PhysRevB.94.075125 (2016), 1604.02394.

[47] M. Zacharias and F. Giustino, Theory of the special displacement method for electronic structure calculations at finite temperature, Physical Review Research **2**, 7 (2020), 1912.10929.

[48] C. E. Patrick and F. Giustino, Unified theory of electron–phonon renormalization and phonon-assisted optical absorption, Journal of Physics: Condensed Matter **26**, 365503 (2014).

[49] A. Miglio, V. Brousseau-Couture, E. Godbout, G. Antonius, Y. H. Chan, S. G. Louie, M. Côté, M. Giantomassi, and X. Gonze, Predominance of non-adiabatic effects in zero-point renormalization of the electronic band gap, npj Computational Materials **6**, 10.1038/s41524-020-00434-z (2020), 2011.12765.

[50] G. Kresse, J. Furthmüller, and J. Hafner, Ab initio Force Constant Approach to Phonon Dispersion Relations of Diamond and Graphite, Europhysics Letters **32**, 729 (1995).

[51] K. Parlinski, Z. Q. Li, and Y. Kawazoe, First-Principles Determination of the Soft Mode in Cubic ZrO_2, Physical Review Letters **78**, 4063 (1997).

[52] V. Kapil and E. A. Engel, A complete description of thermodynamic stabilities of molecular crystals, Proc. Natl. Acad. Sci. U.S.A. **119**, e2111769119 (2022).

[53] S. Sharifzadeh, P. Darancet, L. Kronik, and J. B. Neaton, Low-Energy Charge-Transfer Excitons in Organic Solids from First-Principles: The Case of Pentacene, The Journal of Physical Chemistry Letters **4**, 2197 (2013).

[54] L. Graf, A. Kusber, B. Büchner, and M. Knupfer, Strong exciton bandwidth reduction in pentacene as a function of temperature, Phys. Rev. B **106**, 165429 (2022).

[55] J. Aragó and A. Troisi, Regimes of exciton transport in molecular crystals in the presence of dynamic disorder, Advanced Functional Materials **26**, 2316 (2016).

[56] S. Sharifzadeh, C. Y. Wong, H. Wu, B. L. Cotts, L. Kronik, N. S. Ginsberg, and J. B. Neaton, Relating the Physical Structure and Optoelectronic Function of Crystalline TIPS-Pentacene, Advanced Functional Materials **25**, 2038 (2015).

[57] M. Asher, R. Jouclas, M. Bardini, Y. Diskin-posner, N. Kahn, R. Korobko, A. R. Kennedy, L. S. D. Moraes, G. Schweicher, J. Liu, D. Beljonne, Y. Geerts, and O. Ya, Chemical Modifications Suppress Anharmonic Effects in the Lattice Dynamics of Organic Semiconductors, ACS Materials Au 10.1021/acsmaterialsau.2c00020 (2022).

[58] S. Haas, B. Batlogg, C. Besnard, M. Schiltz, C. Kloc, and T. Siegrist, Large uniaxial negative thermal expansion in pentacene due to steric hindrance, Phys. Rev. B **76**, 1 (2007).

[59] J. P. Perdew, K. Burke, and M. Ernzerhof, Generalized Gradient Approximation Made Simple, Physical Review Letters **77**, 3865 (1996).

[60] H. J. Monkhorst and J. D. Pack, Special points for Brillouin-zone integrations, Phys. Rev. B **13**, 5188 (1976).

[61] A. Tkatchenko and M. Scheffler, Accurate molecular van der Waals interactions from ground-state electron density and free-atom reference data, Physical Review Letters **102**, 6 (2009).

[62] Y. Eldar, M. Lindenbaum, M. Porat, and Y. Y. Zeevi, The Farthest Point Strategy for Progressive Image Sampling, IEEE Transactions on Image Processing **6**, 1305 (1997).

[63] R. J. G. B. Campello, D. Moulavi, A. Zimek, and J. Sander, Hierarchical density estimates for data clustering, visualization, and outlier detection, ACM Trans. Knowl. Discov. Data **10**, 5 (2015).

[64] A. P. Bartók, R. Kondor, and G. Csányi, On representing chemical environments, Phys. Rev. B **87**, 184115 (2013).

[65] M. J. Willatt, F. Musil, and M. Ceriotti, Feature optimization for atomistic machine learning yields a data-driven construction of the periodic table of the elements, Phys Chem Chem Phys **20**, 29661 (2018).

[66] A. Singraber, N2P2, `https://github.com/CompPhysVienna/n2p2`.

[67] V. Kapil, M. Rossi, O. Marsalek, R. Petraglia, Y. Litman, T. Spura, B. Cheng, A. Cuzzocrea, R. H. Meißner, D. M.Wilkins, B. A. Helfrecht, P. Juda, S. P. Bienvenue, W. Fang, J. Kessler, I. Poltavsky, S. Vandenbrande, J. Wieme, and M. Ceriotti, i-PI 2.0: A universal force engine for advanced molecular simulations, Computer Physics Communications **236**, 214 (2018).

[68] S. Plimpton, Fast parallel algorithms for short-range molecular dynamics, J. Compt. Phys. **117**, 1 (1995).